buildings

Article

# Wind-Induced Vibration and Vibration Suppression of High-Mast Light Poles with Spiral Helical Strakes

**Meng Zhang [1], Tianxiang Li [1], Yang Wang [2], Yizhuo Chen [1] and Guifeng Zhao [1,*]**

[1] School of Water Resources and Civil Engineering, Zhengzhou University, Zhengzhou 450001, China
[2] Institute of Civil Engineering, Huzhou Vocational & Technical College, Huzhou 313000, China
* Correspondence: gfzhao@zzu.edu.cn

**Abstract:** In this study, three-dimensional finite element models of high-mast light poles without and with spiral helical strakes were built using ANSYS software to investigate their vibration characteristics in a wind environment. Based on a two-way, fluid–structure interaction simulation method, the dynamic responses of the high-mast light poles under different windspeeds were analyzed. The results indicate that the high-mast light pole structure without spiral helical strakes may suffer from evident vortex-induced vibration, which is dominated by the third vibration mode in the windspeed range of 5~8 m/s, whereas the light pole with spiral helical strakes had no obvious vortex-induced vibration. The external helical strakes can amplify the along-wind response of the light pole to a certain extent, while significantly decreasing its crosswind vortex-induced response. The vibration suppression effect is better when the value of pitch $P$ is small. Practically, if $P = 7.5\ D$ ($D$ is the diameter of the dominant vibration mode), the vibration suppression effect is best. On the other hand, if the value of pitch $P$ remains constant, the vibration suppression effect increases with the height $H$ of the outer helical strakes. However, excessively high outer helical strakes may also increase the along-wind response of the structure. In general, when spiral helical strakes are used in design, the recommended values of $P$ and $H$ are $P = 7.5\ D$ and $H = 0.20\ D$.

**Keywords:** two-way fluid–structure interaction; high-mast light poles; helical strake; wind-induced response; vibration suppression



**Citation:** Zhang, M.; Li, T.; Wang, Y.; Chen, Y.; Zhao, G. Wind-Induced Vibration and Vibration Suppression of High-Mast Light Poles with Spiral Helical Strakes. *Buildings* **2023**, *13*, 907. https://doi.org/10.3390/buildings13040907

Academic Editors: Francisco López Almansa, Chunxu Qu, Jinhe Gao, Rui Zhang, Jiaxiang Li and Ziguang Jia

Received: 21 February 2023
Revised: 23 March 2023
Accepted: 27 March 2023
Published: 29 March 2023



## 1. Introduction

Since the beginning of the 21st century, due to the dramatic increase in traditional energy consumption, strategies to achieve low carbon and new energy development have been established and deployed around the world to overcome energy shortages and dependence on traditional energy [1]. However, even if the current energy demands have been reasonably assessed and planned for future use, the availability of conventional energy will decline rapidly between 2030 and 2040. For the daily life of human beings in this century, how to use energy reasonably is a critical issue in engineering practice [2]. For example, street lighting is one of the most energy-intensive utilities, especially in cities and major roads, and consumes more than one-fifth of the world's electricity annually. With the continued development of society, the proportion of artificial lighting in cities will reach 70% by 2050. Therefore, the modernization and performance improvement of public lighting is becoming an essential lever for sustainable development [3]. For city lighting, high-pole lighting is generally a high-rise structure with a height of 20 m or more. Because of its wide illumination range and vital function, it has been widely used in large stadiums, airports, overpasses and other places in recent years [4]. From a structural point of view, tall lamp poles are characterized by their height, small cross-sectional area and remarkable wind vibration effect. Working in high-altitude outdoor environments for extended periods makes them particularly vulnerable to the effects of natural wind induced vibration. At present, it has been confirmed that the fluid–structure interaction is an important reason for the wind-induced vibration of the high-mast light pole as a highly flexible structure under the excitation of natural wind. During the normal operation of high-mast light poles, there is a potential physical phenomenon called vortex-induced vibration. Vortex-induced vibration occurs when the fluid flows through the bluff body, and the formation and periodic shedding of the vortex will cause the vibration of the bluff body [5]. Once the vibration intensity reaches a certain level, the flow field shedding will be locked, which results in large vibration energy and directly causes fatigue damage and resonance damage to the structure [6–8]. In practical engineering, wind-induced vibration frequently damages tall pole lights and causes significant adverse effects. On 14 February 2003, a light pole in western Illinois collapsed due to wind-induced vibration [9], as shown in Figure 1a. On 12 November 2003, on the I-29 highway in Iowa, several tall pole lights collapsed due to wind-induced vibration on the open ground beside the interstate highway [10]. In China, similar accidents have also occurred occasionally. For example, more than 30 lamp poles tilted and collapsed due to wind events on 19 August 2014 in Nanchang City, Jiangxi Province, as shown in Figure 1b. On 26 June 2018, because of long-term wind-induced vibration, one lamp pole near Guanyin Bridge collapsed in Chengdu City, Sichuan Province. On 5 July 2020, one lamp pole collapsed due to wind-induced vibration in Nanning City, Guangxi Province. From the perspective of energy utilization, to extend the service life of high-mast light poles is to save energy. Therefore, it is of particular importance to conduct detailed dynamic analysis and design of high-mast light poles to ensure that light poles can operate safely within their design service periods.

(**a**) (**b**)

**Figure 1.** Wind-induced vibration collapse accident of high-mast light poles. (**a**) Light pole collapse accident in western Illinois. (**b**) Light pole collapse accident in Nanchang City.

Researchers in China and other countries have performed experimental research and theoretical analysis regarding the wind-induced dynamic response and fatigue damage of high-mast light poles. For example, Zhuge et al. [11] experimentally studied the wind-induced vibration of a 30 m tall pole lamp excited by natural wind. Taplin et al. [12] analyzed a collapse accident of a lamp pole using finite element analysis and field measurements. The results showed that excessive stress fluctuation of the anchor bolts is the main reason for the fatigue failure of the lamp pole. Goode et al. [13] investigated a lamp pole collapse accident and found that the failure was caused by fatigue cracks and propagated under a high-stress cycle. A single wind event probably caused the collapse of the lamp pole. A method was proposed to determine the reliability index of the expected fatigue life of the lamp pole structure by specifying the lamp's surface area, height, diameter and wall thickness. Chien et al. [14] developed a wind-resistant design program for slender conical support structures such as high-mast light poles, which can accurately analyze the gust effect coefficient of the along-wind response and the crosswind vortex-induced vibration response. Chang et al. [15] proposed a general model to analyze the wind-induced vibration of polygonal cylinders based on wind tunnel test results. Dawood et al. [16] evaluated the influence of different parameters on the vibration caused by vortex shedding and natural gusts. They found that the safe service life of a high-mast light pole mainly depends on the effective stress range at the bottom of the pole under wind loads. Peng et al. [17] numerically studied the wind-induced response and fatigue life of a high-mast light pole. Azzam [18] performed a failure analysis of lampposts in seven US states. The results show that the most common failure mode of the lamp rod was fatigue at the base connection under the action of wind-induced vibration. Sherman et al. [19] investigated many in-service high-pole lamps and found fatigue cracks in most of the lamp poles. Based on the survey results and analysis, the fatigue design concept combined with the wind effect was introduced to ensure the safety of high-pole lamps. Zhou et al. [20] analyzed the displacement response and wake characteristics of a circular lamp pole under different windspeeds through wind tunnel tests. In addition to the above research, relevant studies on the fatigue damage of high-rise lamp structures due to wind-induced vibration have also been conducted by Connor [21], Thompson [22] and Counsell [23].

These studies are of great importance for the optimal design of high-mast light poles. However, in practical engineering applications, mitigating or controlling the vibrations of similar high-rise structures has been a common issue around the world. In the fields of industrial and marine structures, spiral side plates are widely used to reduce vortex-induced vibration of structures such as marine risers. A spiral side plate is composed of metal or flexible elastomer ribs and is a typical aerodynamic damper. Its principle is that when the spiral side plate is spirally wound around the structure or component in a certain way, the geometrical shape of the structure is changed, thereby resulting in the different aerodynamic characteristics of the structure. Previous studies [24,25] have shown that the pitch $P$ and the height $H$ of spiral side plates have a great influence on the vortex-induced vibration characteristics of the structure. Regarding the wind-induced vibration behaviors of helical side plates, Zhou et al. [26] conducted wind tunnel tests on rigid cylinders with three-piece helical side plates with pitch $P$ = 10 $D$ and helical height $H$ = 0.12 $D$ ($D$ is the critical diameter of the dominant vibration mode). The results indicate that no frequency locking occurs on cylinders with helical side plates in the windspeed range of 5–8 m/s, which is different from the smooth cylinders. Zhou et al. [27] compared the eddy-induced vibration characteristics of smooth risers and three groups of risers with helical side plates under different Reynolds numbers and found that the vibration response of the transverse direction can be reduced by approximately 70%. Ranjith et al. [28] studied the suppression effect of the helical side plate on the vortex-induced vibration of a cylinder. The analysis shows that the cylinder with an additional helical side plate has a higher drag coefficient, and its response to the vortex-induced vibration is reduced by approximately 99%. Quen et al. [29] conducted a study on the effectiveness of the helical side plate in suppressing vortex-induced vibration of a long flexible cylinder by changing the pitch $P$ and the height $H$ of the helical side plates. Chen et al. [30] analyzed the eddy-induced vibration response of PVC utilizing computational structural dynamics using the bidirectional coupling simulation method. The results showed that the spiral side plates can effectively reduce the vortex shedding frequency, and the lateral vibration response of the PVC tube was significantly decreased by approximately 97%.

In total, it has been demonstrated that helical side plates are an effective means to suppress the vortex-induced vibration response of high-rise circular tube structures. However, to our knowledge, studies of the specific vibration characteristics and influence of the anti-vibration measures of high-mast light poles under wind environments remain limited. Due to the lag of related research, high-mast light pole collapse accidents have occurred frequently in recent years. To address the topics discussed above, in this study, three-dimensional finite element models of high-mast light poles without and with three-plate spiral helical strakes are built using ANSYS software to investigate their vibration characteristics in a wind environment. Based on a two-way fluid–structure interaction simulation method, the dynamic responses of the high-mast light poles under different windspeeds are analyzed. The purpose of this study is to provide technical support for the wind resistance design and daily maintenance of high-mast light pole structures.

## 2. Numerical Simulation Calculation Method for High-Mast Light Poles

### *2.1. Control Equation for Numerical Simulation*

#### 2.1.1. Control Equation of Fluid Dynamics

Fluid flow needs to satisfy the mass conservation equation, momentum conservation equation and energy conservation equation. The mass conservation equation, also known as the continuity equation, is one of the critical control equations in fluid flow. It regards fluid as a continuous medium without voids. The mass conservation equation is expressed as the sum of net mass flowing out of the microelement in a unit of time equal to the sum of net mass flowing into the microelement in the same time interval. Its differential equation expression is as follows:

$$\widetilde{D} = div\vec{V} = \frac{\partial u}{\partial x} + \frac{\partial v}{\partial y} + \frac{\partial w}{\partial z} = 0 \tag{1}$$

In the formula, $u$, $v$ and $w$ represent the components of the fluid in the $x$, $y$ and $z$ directions, respectively.

The law of conservation of momentum is essentially Newton's second law. The law of conservation of momentum is expressed as the rate of change in fluid momentum with time in a microcellular body, which is equal to the sum of all forces acting on the microcellular body by external forces. The expression of the differential equation is as follows:

$$\frac{\partial \vec{V}}{\partial t} + \vec{V} \cdot \nabla \vec{V} = \vec{f} - \frac{\nabla p}{\rho} + v\nabla^2 \vec{V} \tag{2}$$

where $f$ is the mass force acting on the fluid in all directions, i.e., $x$, $y$ and $z$.

The law of conservation of energy is essentially the first law of thermodynamics, which must be satisfied by a flow system containing heat exchange. The law of conservation of energy is expressed as the increased rate of energy in the microelement being equal to the sum of net heat flow into the microelement, volume force and area force acting on the microelement. The energy conservation equation can be written as follows:

$$\frac{\partial(\rho T)}{\partial t} + div(\rho u T) = div\left(\frac{k}{c_p} \bullet gradT\right) + S_T \tag{3}$$

where $T$ is the thermodynamic temperature, $k$ is the heat transfer coefficient of the fluid, $c_p$ is the specific heat capacity, $S_T$ is the viscous dissipative term, *div* is a divergence operator, *grad* is a gradient operator and $\bullet$ is a separator.

#### 2.1.2. Control Equation of Solid Mechanics

The governing equation of wind-induced vibration of the structure is:

$$M_s \bullet \frac{d^2 r}{dt^2} + C_s \bullet \frac{dr}{dt} + K_s \bullet r + \tau_s = 0 \tag{4}$$

where $M_S$ is the solid mass matrix, $C_S$ is the solid damping matrix, $K_S$ is the solid stiffness matrix, $r$ is the solid displacement and $\tau_s$ is the Cauchy stress tensor for solids.

#### 2.1.3. Fluid–Solid Coupling Control Equation

Fluid–solid coupling follows the most fundamental conservation equation. The interface of fluid–solid coupling satisfies the conditions of stress, displacement, heat flux and temperature conservation of the fluid and structure. The governing equation is shown in Equation (5).

$$\begin{cases} \tau_f \cdot n_f = \tau_s \cdot n_s \\ d_f = d_s \\ q_f = q_s \\ T_f = T_s \end{cases} \tag{5}$$

where $\tau$ is stress, $d$ is displacement, $q$ is the heat flow rate and $T$ is temperature. The subscript $f$ represents the fluid boundary at the interface of fluid–solid coupling, and the subscript $s$ represents the solid boundary at the interface of fluid–solid coupling.

### 2.2. Calculation Method

Based on the ANSYS Workbench platform and using the Transient Structural + Fluent + System Coupling module, the numerical simulation method of bidirectional fluid–solid coupling is used to solve and analyze the bidirectional fluid–solid coupling of a high-pole lamp structure. Figure 2 shows the connection between modules using ANSYS software to solve fluid–solid coupling problems. Figure 3 demonstrates a flow chart for calculating the bidirectional fluid–solid coupling problem.

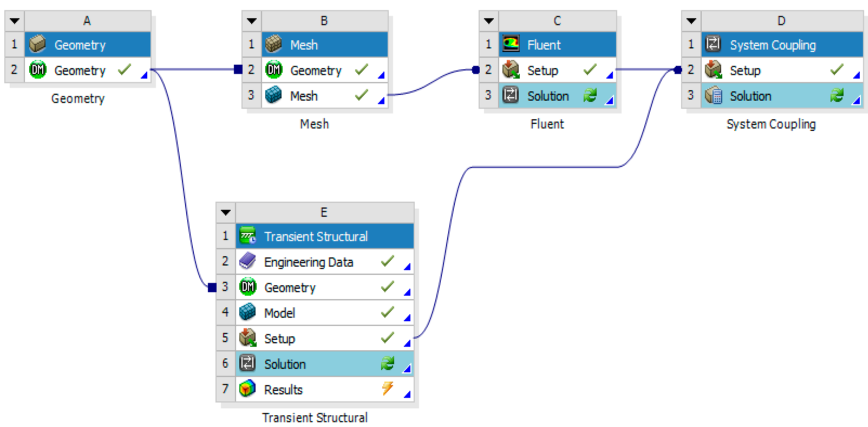


**Figure 2.** Two-way fluid–solid coupling calculation setting diagram.

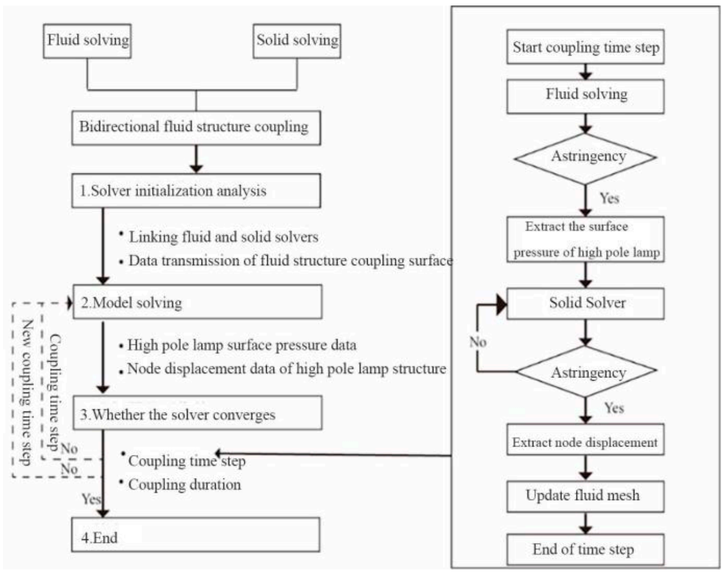


**Figure 3.** Flow chart for bidirectional fluid–solid coupling calculation.

## 3. Numerical Model for High-Mast Light Pole and Wind-Induced Vibration Analysis

### *3.1. Establishment of the Finite Element Model for a High-Mast Light Pole*

Considering the calculation amount, calculation accuracy and actual structural characteristics of the whole structure, some details of the high-mast light pole structure are ignored in the finite element analysis model. Figure 4 shows the structural sketch of the high-mast light pole. The lamp pole is 36.6 m in height, and its section is hexagonal. It is plugged from three sections of variable cross-section Q235B round steel pipes. The diameters and thicknesses of the pipe sections from bottom to top are 0.58 m, 8 mm, 0.44 m, 8 mm, 0.31 m, 6 mm and 0.18 m, 6 mm, respectively. The weights of the lamp pole and the top lamp are 2388 kg and 272 kg, respectively.

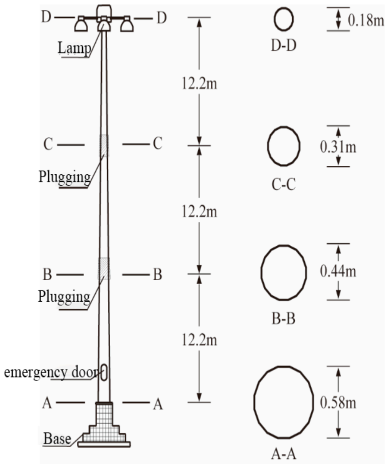


**Figure 4.** Structural schematic diagram.

The sideview of the light pole is shown in Figure 5, and the simplified geometric model diagram is demonstrated in Figure 6. The plug-in part, safety door and other detailed structures are ignored during the model-building process. Due to the large mass of the lamp, its impact on the dynamic characteristics of the light pole cannot be ignored. In this paper, the lamp is simplified as a round plate with a diameter of 2.4 m, the mass is the same as the actual structure and the cross-section of the lamp pole is simplified as a circle during the model-building process.

**Figure 5.** High pole lamp scene diagram.

**Figure 6.** Geometric model.

## 3.2. Fluid Numerical Model

### 3.2.1. Boundary Conditions of CFD Simulation

To obtain the force characteristics of the light pole under wind load, the fluid domain mesh is set around the light pole, as shown in Figure 7. The size of the calculation area along the wind direction is 35 *d*, in which the lengths of the upstream inflow area and downstream wake area of the light pole are 10 *d* and 25 *d*, respectively. The crosswind calculation domain is 20 *d* in size, and the span lengths on both sides are 10 *d*, of which *d* is 0.58 m in diameter at the bottom of the tall pole lamp. The calculated domain size along the height direction is 2 *h* (*h* is the height of the pole). For the solution of CFD problems, boundary conditions need to be defined. In this study, the primary boundary conditions include the inlet boundary condition, outlet boundary condition, symmetric boundary condition and wall boundary condition.

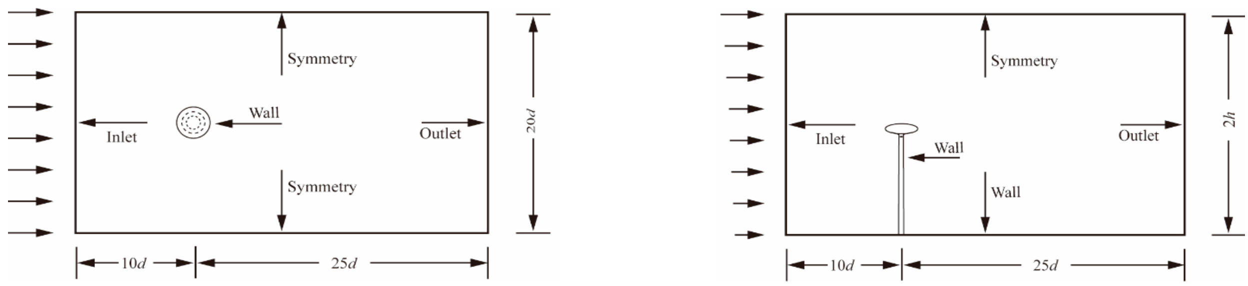


**Figure 7.** Schematic diagram of the calculation domain size and boundary conditions.

Inlet boundary conditions (inlet): The left-hand side boundary along the wind direction is set as the velocity inlet boundary condition, and the UDF custom function is used to define the average wind profile to take into account the variation in windspeed along the height direction. Outlet boundary condition (outlet): The pressure value is atmospheric pressure, and the right side boundary along the wind is set as the pressure outlet boundary. Symmetry: The top of the computational domain and the boundary along both sides of the transverse wind direction are set with symmetrical boundary conditions. Wall boundary condition: The surface of the pole is set as a nonslip wall condition. Similarly, the bottom of the calculation domain is used to simulate the ground and is also set as a nonslip wall condition, regardless of the roughness of the ground.

3.2.2. Flow Field Model Meshing

The meshing of the entity model adopts the nonuniform scheme for precision and less calculation. The encrypted area is set around the lamp pole when meshing. Figure 8 demonstrates the side view and top view of the calculation domain grid. From Figure 8, we can see that the semicircular encrypted area with a diameter of 6 m and a height of 40 m and rectangular encrypted area with length, width and height of 9 m, 6 m and 40 m are set around the lamp pole.

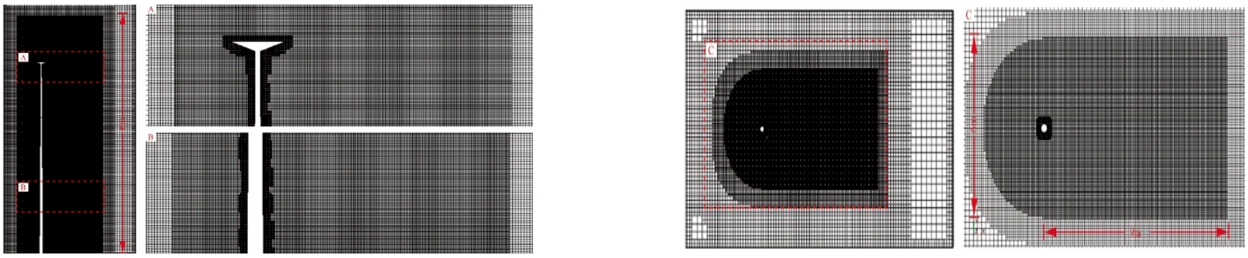

(**a**) Side view of the computational domain grid (**b**) Top view of the computational domain grid

**Figure 8.** Computing the domain grid of the light pole.

*3.3. Modal Analysis*

The modal analysis of the lamp pole was carried out, and the first four orders of vibration patterns of the structure were obtained by using the Lanczos method with full restraint on the base of the lamp pole without applying prestress. Figure 9 shows the first four modes of the structure with natural frequencies of 0.36 Hz, 1.59 Hz, 4.03 Hz and 7.80 Hz, respectively. As demonstrated in Figure 9, the lamp pole exhibits translation vibrations in the X and Y directions under the first two vibration modes. The difference is that the first vibration mode is mainly in the X-direction, whereas the second vibration mode is the combination of X-direction and Y-direction translation movements. The third and fourth modes are mainly torsional vibration modes. The third mode is the combination of X-direction translation movement and torsional movement, whereas the fourth mode is the combination of X-direction translation movement, Y-direction translation movement and torsional movement.

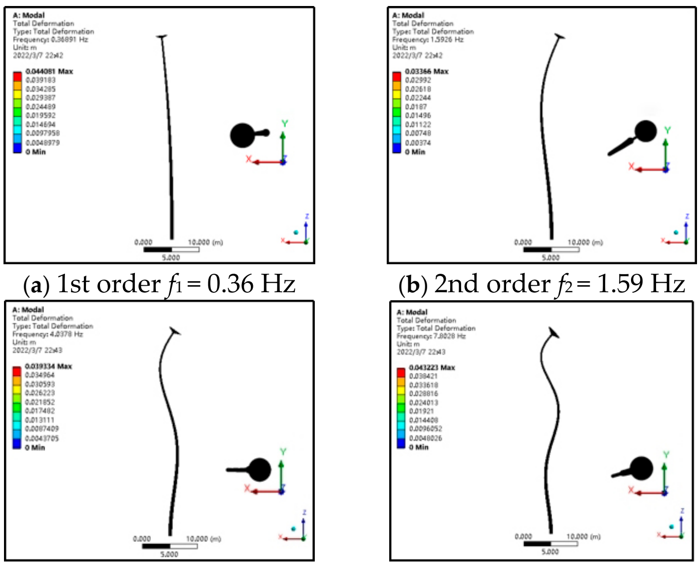


(**a**) 1st order $f_1 = 0.36$ Hz (**b**) 2nd order $f_2 = 1.59$ Hz
(**c**) 3rd order $f_3 = 4.03$ Hz (**d**) 4th order $f_4 = 7.80$ Hz

**Figure 9.** The first four vibration modes of the light pole structure.

Table 1 presents a comparison of the results for the simulated natural frequencies given by the finite element analysis in this study and the results of the vibration modes of the light pole, as referenced (Aheran et al.) [31]. The finite element simulation results in this study are highly in agreement with the values in the reference (Aheran et al.) [31], and the maximum deviation is less than 7%, which indicates that the established finite element model in this study is reliable and can be used to simulate more engineering cases.

**Table 1.** Comparison of the simulated natural frequencies and the results given by reference (Aheran et al.).

| Mode Order | Simulated Frequency in the Present Study (Hz) $f_0$ | Frequency Results Given by Reference (Aheran et al.) (Hz) $f$ | Relative Deviation (%) $\lvert(f_0 - f)/f_0\rvert$ |
|---|---|---|---|
| 1 | 0.36 | 0.35 | 2.86 |
| 2 | 1.59 | 1.50 | 6.00 |
| 3 | 4.03 | 3.80 | 6.05 |
| 4 | 7.80 | 7.50 | 4.00 |

3.3.1. Vibration Mode Analysis

Figure 10 demonstrates the normalized deflections of the first four modes. As shown in Figure 10, the first mode is evident at any position along the length of the pole, whereas the second mode deflects at 23 m, the third mode deflects twice at 14 m and 30 m, and the fourth mode deflects three times.

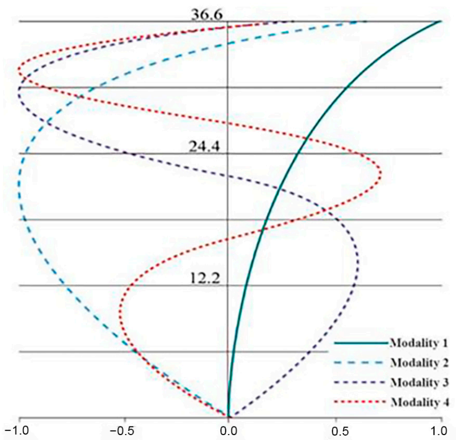


**Figure 10.** Modal deflection normalization.

3.3.2. Critical Windspeed

The critical windspeed $V_c$ is the speed at which lock-in occurs [32]. Polygon sections can be determined by the following formula:

$$V_c = \frac{f_n D}{S} \tag{6}$$

where $f_n$ is the natural frequency of the structure, $D$ is the characteristic size of the object perpendicular to the average velocity and $S$ is the Strouhal number.

The critical windspeed is also called the locking windspeed. According to the above modal analysis results, the maximum displacement of each mode can be obtained. Taking these node positions as the critical diameter of each mode, the critical windspeed of each mode can be calculated according to Formula (6). The results are listed in Table 2.

**Table 2.** Critical Windspeed.

| Position | Height (m) | Critical Diameter (m) | Critical Windspeed (m/s) | | | |
|---|---|---|---|---|---|---|
| | | | Mode 1 | Mode 2 | Mode 3 | Mode 4 |
| 4-1 | 9.75 | 0.48 | | | | 20.80 |
| 3-1 | 14.00 | 0.43 | | | 9.63 | |
| 4-2 | 22.00 | 0.34 | | | | 14.73 |
| 2-1 | 23.00 | 0.33 | | 2.92 | | |
| 3-2 | 30.00 | 0.26 | | | 5.82 | |
| 4-3 | 31.70 | 0.23 | | | | 9.97 |
| 1-1 | 36.60 | 0.18 | 0.36 | | | |

#### 3.3.3. Monitoring Points

To analyze the dynamic response characteristics of the light pole structure under wind loads, three monitoring points are set on the finite element model to record the stress and displacement responses, as shown in Figure 11. The locations of the monitoring points can be determined by the vibration mode of the light pole structure. According to the results in Section 3.3.1, the maximum deflection of mode 1 is at the top of the pole structure, and the vibration along the length of the pole gradually increases. Meanwhile, the occurrence probability of mode 4, as a higher-order mode, is relatively low. Therefore, the deflections of mode 1 and mode 4 are not adopted as monitoring points in this study. Modal 2 deflects at 23 m from the bottom of the pole, and modal 3 deflects at 14 m and 30 m from the bottom of the pole. Therefore, the positions at 30 m, 23 m and 14 m from the bottom of the pole are taken as monitoring points to analyze the wind-induced vibration dynamic response of the structure.

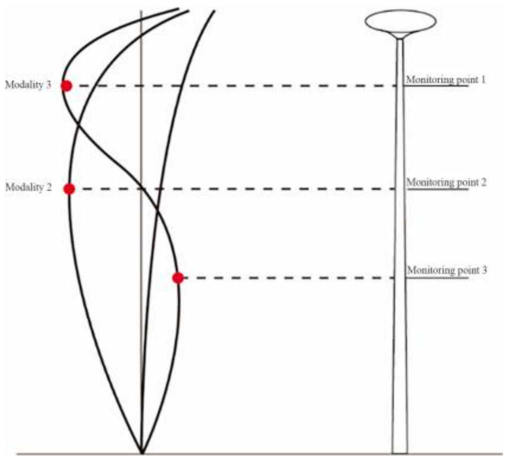


**Figure 11.** Location of measuring points.

### *3.4. Grid Sensitivity Analysis*

To ensure that the calculation results are less affected by the grid size, three grid setting schemes, namely, dense grid, medium grid and coarse grid, are selected to discretize the calculation domain. Taking monitoring point 1 as an example, a grid sensitivity analysis concerning the difference between the maximum displacements of the pole under windspeed 12 m/s is performed. The results are presented in Table 3. From the data in the table, it can be seen that the maximum difference in displacement at monitoring point 1 under the dense grid and coarse grid conditions is 5.43%. The maximum difference in displacement at monitoring point 1 under dense grid and medium grid conditions is only 1.37%. In general, the relative deviation is within the acceptable range under the conditions of dense grid, medium grid and coarse grid. After comprehensive consideration of the calculation accuracy and efficiency, the medium-density grid scheme is used in this study for subsequent calculations.

**Table 3.** Setting Parameters of Different Grid Schemes.

| Grid Scheme | Boundary Layer Grid Thickness (mm) | Global Grid Size (mm) | Light Pole Surface Grid Size (mm) | Encrypted Area Grid Size (mm) | Maximum Displacement at Monitoring Point 1 (mm) | Relatively Dense Grid Deviation (%) |
|---|---|---|---|---|---|---|
| Coarse grid | 8 | 40 | 8 | 8 | 44.27 | 5.33 |
| Medium grid | 4 | 25 | 5 | 5 | 46.63 | 1.37 |
| Dense grid | 2 | 10 | 2 | 2 | 46.99 | / |

## *3.5. Wind Vibration Response Analysis of Smooth High Light Pole Structure*

### 3.5.1. Displacement Response Analysis

According to the measured windspeed at the location of the high pole lamp structure, as in the reference Aheran et al. [31], this paper selects 12 windspeed conditions with windspeeds of 1 to 12 m/s with increments of 1 m/s for the simulation calculation. Figure 12 shows the root mean square value of the displacement response of the high light pole structure under different windspeeds and directions.

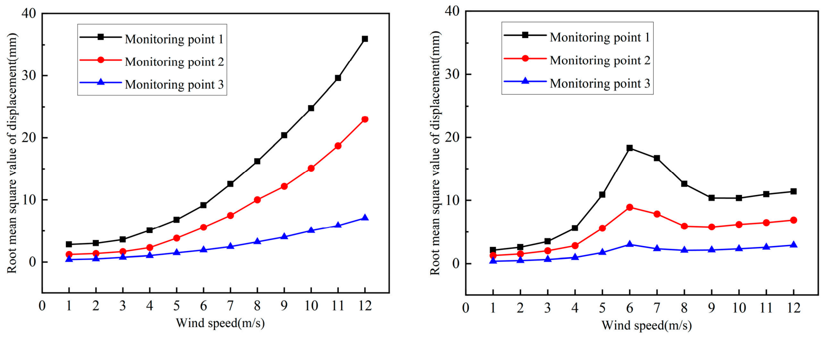


(**a**) Along-wind (**b**) Crosswind

**Figure 12.** Root mean square value of displacement responses of the smooth light pole structure.

As demonstrated in Figure 12a, the displacements at the monitoring points increase monotonically as the windspeed increases, and there is no significant amplitude change. In addition, when the windspeed gradually increases from 1 m/s to 12 m/s, the growth rate of the root mean square value of the displacements of the structure also increases. The maximum displacements at monitoring points 1, 2 and 3 are 35.9 mm, 23.0 mm, and 7.1 mm, respectively. Figure 12b shows that the displacements at all the monitoring points fluctuate significantly within the windspeed range of 5~8 m/s, which indicates that vortex-induced vibration occurs. In particular, when the windspeed approaches 6 m/s, the root mean square value of the displacement at each monitoring point reaches its maximum value, i.e., 18.3 mm at monitoring point 1, 8.9 mm at monitoring point 2, and 3.0 mm at monitoring point 3.

### 3.5.2. Analysis of Wake Shedding Frequency

According to the above displacement response results, one can find that significant vortex-induced vibration occurs when the windspeed is 6 m/s, and the largest displacement response is at monitoring point 1. Therefore, the acceleration response at monitoring point 1 is converted from the time–history analysis to the frequency domain analysis using fast Fourier transform (FFT) to reveal more vibration characteristics of the structure under a windspeed of 6 m/s. Figures 13 and 14 demonstrate the time history and spectrum analysis results of the along-wind acceleration response and crosswind acceleration response at monitoring point 1, respectively.

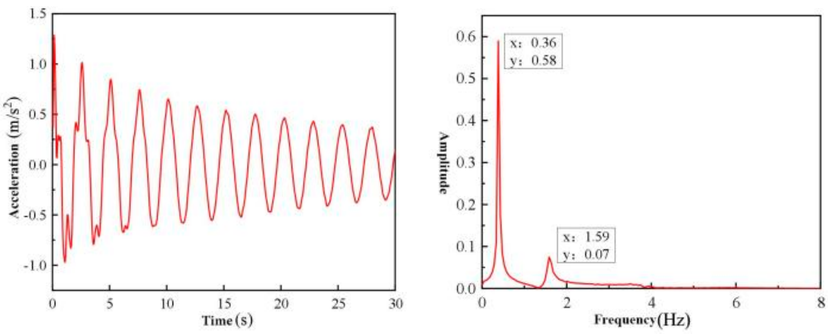


(**a**) Time-history result (**b**) Fourier spectrum result

**Figure 13.** Along-wind acceleration response at monitoring point 1 under a windspeed of 6 m/s.

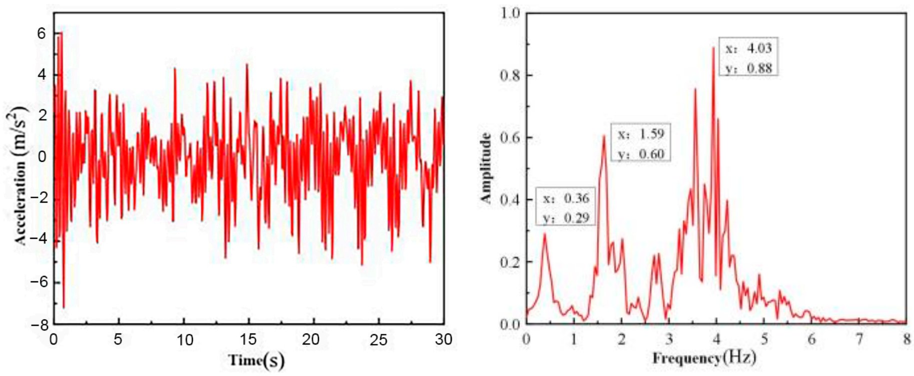


(**a**) Time-history result (**b**) Fourier spectrum result

**Figure 14.** Crosswind acceleration response at monitoring point 1 under a windspeed of 6 m/s.

As indicated in Figure 13, the along-wind acceleration response is dominated by the first-order vibration mode of the structure, with a small part of the second-order vibration mode participating under a windspeed of 6 m/s, which corresponds to the maximum vibration amplitude in the crosswind direction. However, for the crosswind acceleration response at monitoring point 1, the high-order vibration modal (i.e., the third mode, $f$ = 4.03 Hz) contributes more than the low-order vibration modes. According to Formula (6), the wake-shedding frequency can be calculated as $f_s = 0.18 \times 6/0.26 = 4.15$ Hz, which is very close to the third modal frequency of the structure (i.e., $f$ = 4.03 Hz). This result also verifies the correctness of the numerical model built in this study.

## 4. Wind-Induced Vibration Analysis of High-mast Light Poles with Spiral Helical Strakes

The above analysis results show that the smooth high-mast light pole structure is mainly affected by the crosswind vortex-induced vibration within the windspeed range of 5~8 m/s during its service period, which may cause damage or failure of the structure. Therefore, in the following study, the influences of spiral helical strakes on the wind-induced vibration response of high-mast light poles are analyzed.

### *4.1. Basic Parameters and Layout of Spiral Helical Strakes*

There are many factors that may affect the characteristics of vibration suppression of spiral helical strakes, such as the geometric size, surface roughness, coverage length, drag force performance, flow field characteristics, Reynolds number and surrounding structure, among which the geometric size of spiral helical strakes is the most significant factor. The geometric dimensions of spiral helical strakes mainly include pitch, height and start number. Among them, the pitch refers to the length of the spiral helical strakes rotating 360° around the axial direction of the pole. The height of a strake refers to the size of the strake along the radial direction of the pole. The commonly used start number type of spiral helical strakes includes the three-piece type and four-piece type. Previous research [33] has shown that the above two types have no obvious impact on the suppression effect of the structure. Therefore, in this study, a three-piece type is adopted to suppress the vibration of high-mast light poles. The geometric dimension of the spiral side plate is demonstrated in Figure 15.

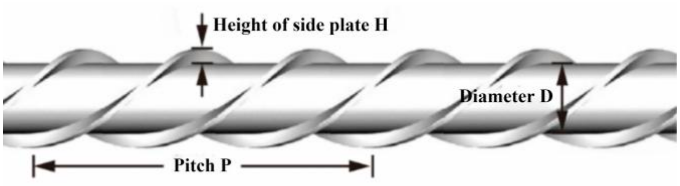


**Figure 15.** Schematic diagram of the geometric dimensions of spiral helical strakes.

According to the wind-induced vibration responses of the pole, the dominant vibration mode is concentrated in the third mode of the structure. Therefore, the upper end of the spiral side plate is arranged 33 m from the bottom of the pole, and the lower section is set 27 m from the bottom of the pole, covering the critical diameter of the third mode of the high pole lamp, as shown in Figure 16.

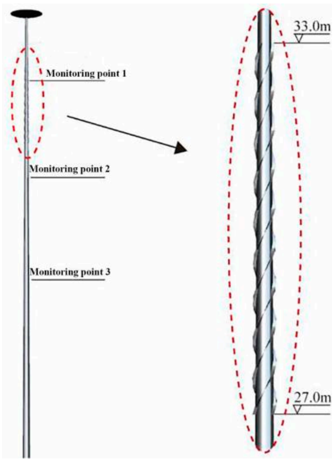


**Figure 16.** Elevation layout of spiral helical strakes.

### *4.2. Influence of Different Pitch on Wind-Induced Vibration Response of the High-Mast Light Pole*

#### 4.2.1. Simulated Conditions

According to the literature [34], the vortex-induced vibration can be effectively suppressed when the spiral side plate is set as three equiangular spacing ribs with side plate height $H$ = 0.1 $D$ and pitch $P$ = 15 $D$. In this section, the side plate height $H$ = 0.10 $D$ ($D$ is the critical diameter of the third mode 0.26 m) is taken as the invariant, while the pitch $P$ is changed from 7.5 $D$ to 17.5 $D$, as shown in Figure 17. The different pitch conditions in the comparison include the following: 7.5 $D$, 10 $D$, 12.5 $D$, 15 $D$ and 17.5 $D$. To facilitate the identification of pitch in the following analysis, the following symbols are used: H0.10D_P7.5D, H0.10D_P10D, H0.10D_P12.5D, H0.10D_P15D and H0.10D_P17.5D.

H0.10D_P7.5D H0.10D_P10D H0.10D_P12.5D H0.10D_P15D H0.10D_P17.5D

**Figure 17.** Different pitches of the high-mast light pole with spiral side plates.

#### 4.2.2. Modal Analysis

Figure 18 shows the vibration modes of the first four orders of the H0.10D_P7.5D light pole obtained from the FE simulation. A comparison of Figures 9 and 18 shows that the shapes of the vibration modes of the high-mast light pole without and with spiral helical strakes are very similar.

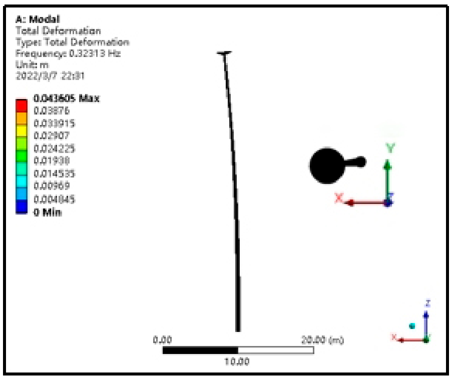


(**a**) 1st order $f_1 = 0.32$ Hz

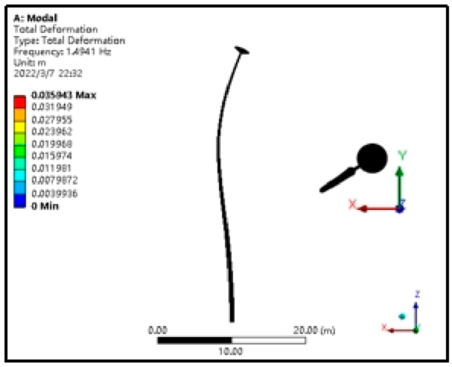


(**b**) 2nd order $f_2 = 1.49$ Hz

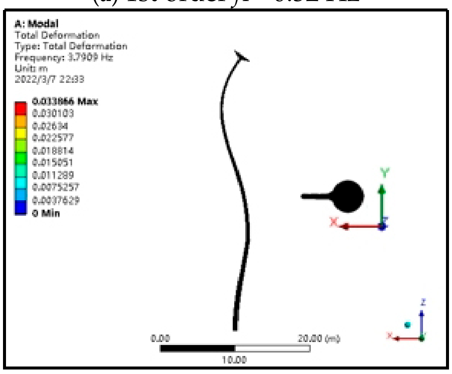


(**c**) 3rd order $f_3 = 3.79$ Hz

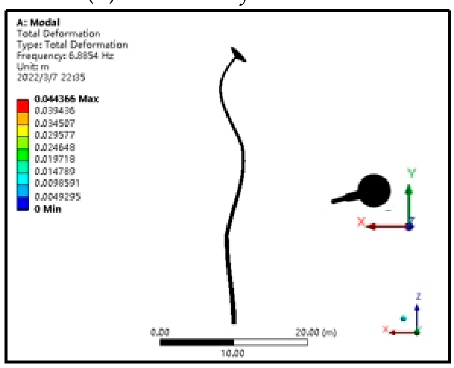


(**d**) 4th order $f_4 = 6.89$ Hz

**Figure 18.** Modes of vibration of the H0.10D_P7.5D light pole of the first four orders obtained from FE simulation.

The natural frequencies of the first four orders of the light pole without and with spiral helical strakes are listed in Table 4. The natural vibration frequencies of the light pole with spiral helical strakes obtained from the FE simulation are in relatively good agreement with the values of the light pole without spiral helical strakes, with the largest difference being approximately 11.66%. This also indicates that the light pole with spiral helical strakes model constructed in this work and the flow field and boundary conditions selected for wind-induced vibration calculation are reasonable.

**Table 4.** Comparison of the first four-mode frequencies of the light pole under different pitch conditions.

| Mode Order | Frequency of Light Pole without Spiral Helical Strakes (Hz) $f_0$ | Frequency of Light Pole with Spiral Helical Strakes (Hz) $f$ | | | | | Maximum Relative Deviation (%) $\lvert(f - f_0)/f_0\rvert$ |
|---|---|---|---|---|---|---|---|
| | | H0.10D_ P7.5D | H0.10D_ P10D | H0.10D_ P12.5 | H0.10D_ P15D | H0.10D_ P17.5D | |
| 1 | 0.36 | 0.32 | 0.36 | 0.35 | 0.35 | 0.35 | 8.33 |
| 2 | 1.59 | 1.49 | 1.56 | 1.57 | 1.49 | 1.53 | 6.29 |
| 3 | 4.03 | 3.79 | 3.98 | 3.93 | 3.97 | 3.99 | 5.96 |
| 4 | 7.80 | 6.89 | 7.44 | 7.46 | 7.26 | 7.42 | 11.66 |

## 4.3. Displacement Response Analysis

### 4.3.1. Along-wind Response

Figure 19 shows the root mean square value of the along-wind displacement response at the monitoring points of the high light pole structure with different spiral helical strake pitches under different wind speeds.

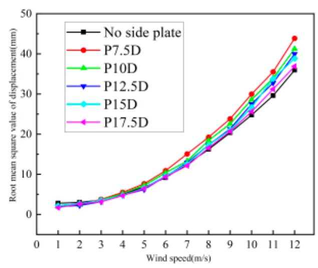


(**a**) Displacement response at monitoring point 1

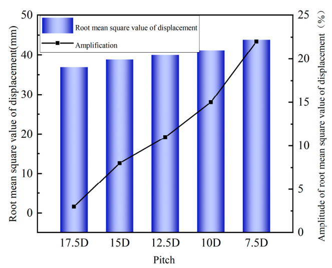


(**b**) Rate of change in response at monitoring point 1 under the windspeed of 12 m/s

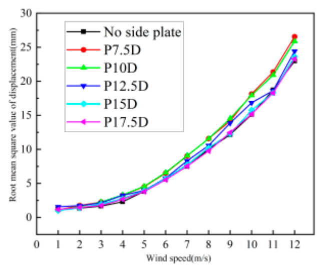


(**c**) Displacement response at monitoring point 2

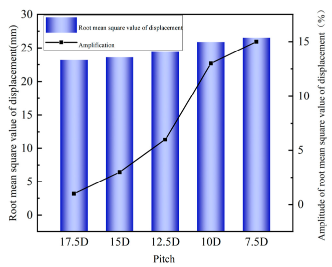


(**d**) Rate of change in response at monitoring point 2 under the windspeed of 12 m/s

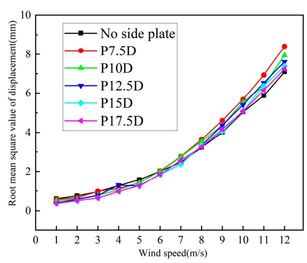


(**e**) Displacement response at monitoring point 3

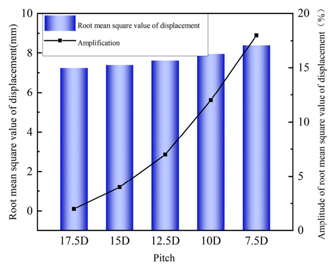


(**f**) Rate of change in response at monitoring point 3 under the windspeed of 12 m/s

**Figure 19.** Root mean square value of the along-wind displacement response at the monitoring points of the high light pole structure under different pitch conditions.

Figure 19 shows that the trends of the along-wind root mean square displacement response of the light pole with different side-plate pitches are basically the same. By and large, spiral side plates may lead to an increase in the along-wind vibration response of the structure. When the incoming windspeed reaches 12 m/s, the root mean square value of the along-wind displacement of the pole without side plates reaches the maximum, with the value of monitoring point 1 being 35.9 mm, the value of monitoring point 2 being 23.0 mm, and the value of monitoring point 3 being 7.1 mm. Under the same windspeed of 12 m/s, the rate of change in responses at different monitoring points has varying degrees of increase.

#### 4.3.2. Crosswind Response

The vortex-induced vibration of the pole structure mainly occurs in the crosswind direction. The root mean square values of the crosswind displacement response at the monitoring points of the high light pole structure under different windspeeds are demonstrated in Figure 20.

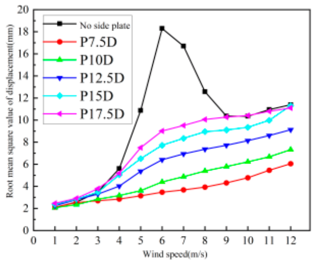


(**a**) Displacement response at monitoring point 1

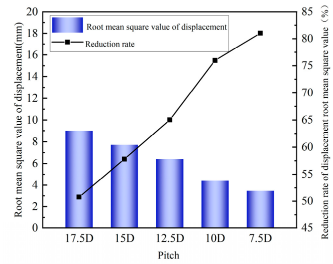


(**b**) Rate of change in response at monitoring point 1 under the windspeed of 6 m/s

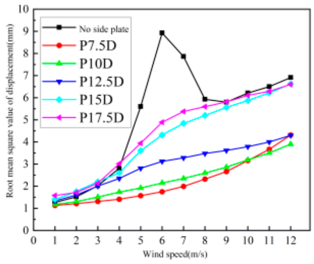


(**c**) Displacement response at monitoring point 2

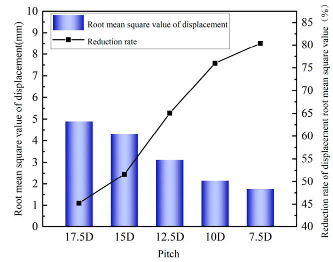


(**d**) Rate of change in response at monitoring point 2 under the windspeed of 6 m/s

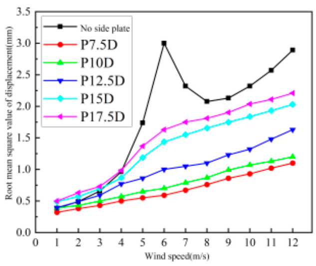


(**e**) Displacement response at monitoring point 3

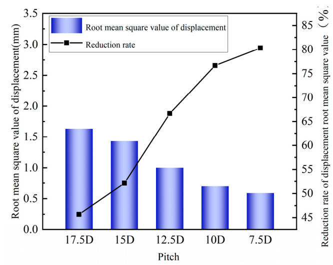


(**f**) Rate of change in response at monitoring point 3 under the windspeed of 6 m/s

**Figure 20.** Root mean square value of the crosswind displacement response at the monitoring points of the high light pole structure under different pitch conditions.

As shown in Figure 20, the changing trends of the crosswind root mean square displacement response of the light pole with different side-plate pitches are basically the same. Comparing the curves of the root mean square displacement results in Figure 20, there are no significant turning points on the curves, which indicates that there is no obvious vortex-induced vibration. This proved that the spiral side plates have a good effect on suppressing crosswind vortex-induced vibration.

The above analysis results also indicate that when the incoming windspeed reaches 12 m/s, the along-wind displacement of the light pole, whether with or without spiral side plates, reaches its maximum value, especially at monitoring point 1. Figure 21 shows the comparison of the amplification ratio of the along-wind displacement response of the light pole under different pitch conditions when the windspeed is 12 m/s. Here, the amplification ratio is defined as the ratio of the root mean square value of displacement at monitoring point 1 under various pitch conditions to the values of the corresponding light pole without spiral side panels. The red line in Figure 21 represents the baseline for comparing the root mean square value of the along-wind displacement response of the light pole under different pitch conditions.

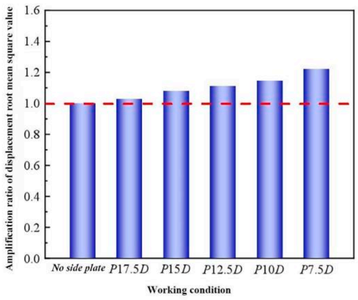


**Figure 21.** Along-wind displacement response at monitoring point 1 under a windspeed of 12 m/s and different pitch conditions.

For the crosswind displacement of the light pole without a side plate, when the incoming windspeed reaches 6 m/s, vortex-induced vibration occurs, and the crosswind displacement response of the light pole without a side plate reaches its maximum value, especially at monitoring point 1. However, for the light pole with side plates, the crosswind displacement responses of the light pole gradually increase with increasing windspeed, and there is no obvious vortex-induced vibration. When the windspeed is 6 m/s, the comparison of the control ratio of the crosswind displacement response of the light pole under different pitch conditions is shown in Figure 22. Similarly, the control ratio here is defined as the ratio of the root mean square value of displacement at monitoring point 1 under various pitch conditions to the values of the corresponding light pole without spiral side panels. The red line in Figure 22 represents the baseline for comparing the root mean square value of the crosswind displacement response of the light pole under different pitch conditions.

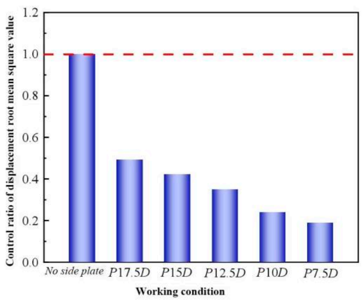


**Figure 22.** Crosswind displacement response at monitoring point 1 under a windspeed of 6 m/s and different pitch conditions.

A comparison of Figures 21 and 22 shows that with the decrease in pitch, the along-wind displacement response of the light pole increases slowly, whereas the crosswind displacement response of the light pole significantly decreases to a low level. In addition, for the same pitch condition, the control ratio of the spiral side plate to the crosswind response is larger than the amplification ratio to the along-wind response of the structure. Therefore, on the whole, a smaller pitch is more favorable for preventing wind-induced damage to the light pole structure. In practical engineering, the pitch $P$ = 7.5 $D$ is a good candidate for the design of vibration attenuation of similar high-mast light pole structures.

### *4.4. Influence of Different Side Plate Heights on the Wind-Induced Vibration Response of the High-Mast Light Pole*

#### 4.4.1. Simulated Conditions

In this section, the pitch $P$ = 15 $D$ is taken as the invariant, and the spiral side plate height $H$ is changed from 0.10 $D$ to 0.25 $D$, as shown in Figure 23. The different spiral side plate height conditions in the comparison include the following: 0.10 $D$, 0.15 $D$, 0.20 $D$ and 0.25 $D$. Similarly, to facilitate the identification of pitch in the following analysis, the following symbols are used: P15D_H0.10D, P15D_H0.15D, P15D_H0.20D and P15D_H0.25D. Among them, the structural form P15D_H0.10D is the same as the abovementioned structural form H0.1D_P15D.

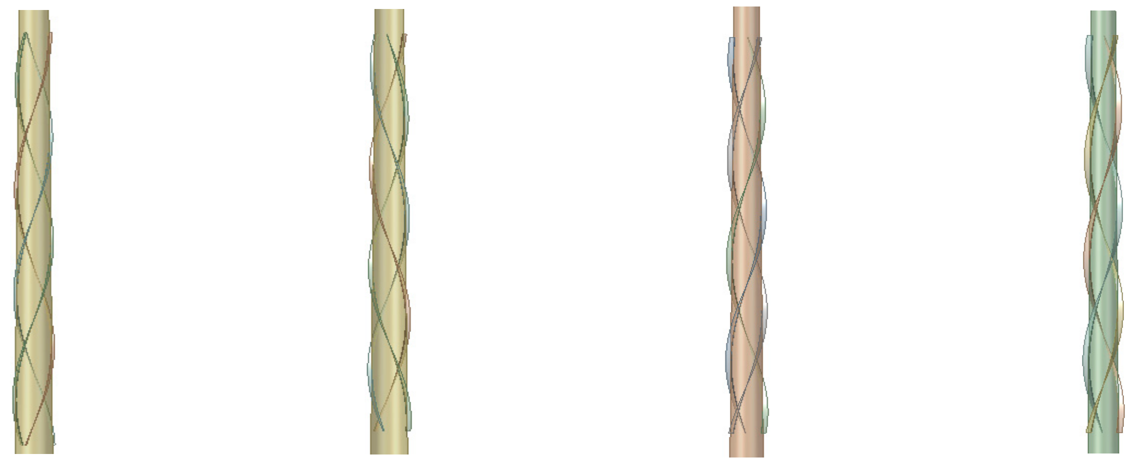


**Figure 23.** Different side plate heights of the high-mast light pole with spiral side plates.

#### 4.4.2. Modal Analysis

Figure 24 demonstrates the vibration modes of the first four orders of the P15D_H0.25D light pole obtained from the FE simulation. It is easy to see that the shapes of the vibration modes of the high-mast light pole look much like the vibration modes shown in Figures 9 and 18. Similarly, the natural frequencies of the first four orders of the light pole without and with spiral helical strakes are presented in Table 5.

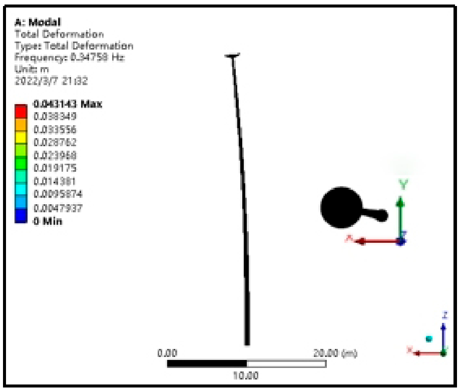


(**a**) 1st order $f_1 = 0.35$ Hz

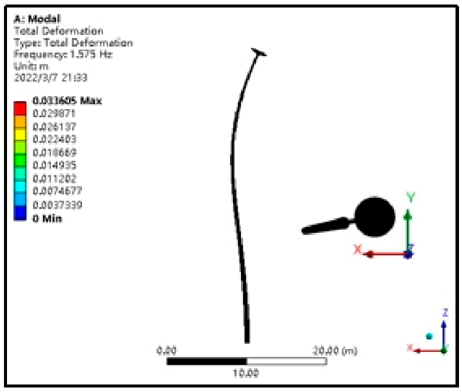


(**b**) 2nd order $f_2 = 1.57$ Hz

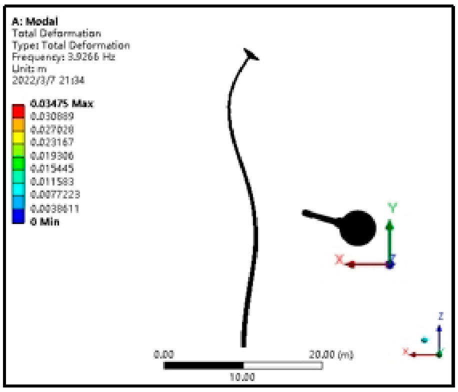


(**c**) 3rd order $f_3 = 3.92$ Hz

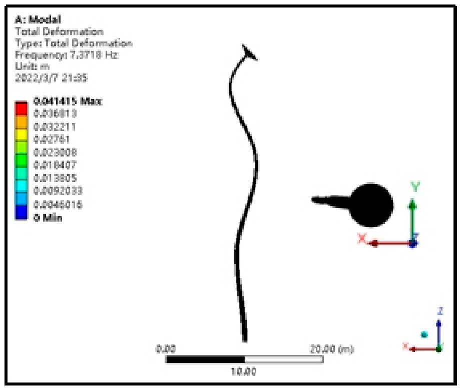


(**d**) 4th order $f_4 = 7.37$ Hz

**Figure 24.** Modes of vibration of the P15D_H0.25D light pole of the first four orders obtained from FE simulation.

**Table 5.** Comparison of the first four-mode frequencies of the light pole under different side plate height conditions.

| **Mode Order** | **Frequency of Light Pole without Spiral Helical Strakes (Hz)** $f_0$ | **Frequency of Light Pole with Spiral Helical Strakes (Hz)** $f$ | | | | **Maximum Relative Deviation (%)** $\lvert(f_0 - f)/f_0\rvert$ |
|---|---|---|---|---|---|---|
| | | **P15D_ H0.10D** | **P15D_ H0.15D** | **P15D_ H0.20D** | **P15D_ H0.25D** | |
| 1 | 0.36 | 0.35 | 0.34 | 0.35 | 0.35 | 5.56 |
| 2 | 1.59 | 1.49 | 1.44 | 1.57 | 1.57 | 9.43 |
| 3 | 4.03 | 3.97 | 3.97 | 3.90 | 3.92 | 3.23 |
| 4 | 7.80 | 7.26 | 7.07 | 7.08 | 7.37 | 9.36 |

Figure 24 and Table 5 show that the natural vibration frequencies of the light pole with spiral helical strakes obtained from the FE simulation are in relatively good agreement with the values of the light pole without spiral helical strakes, with the largest difference being approximately 9.43%. This once again indicates that the light pole with spiral helical strakes model constructed in this work and the flow field and boundary conditions selected for wind-induced vibration calculation are reasonable.

## *4.5. Displacement Response Analysis*

### 4.5.1. Along-Wind Response

The root mean square values of the along-wind displacement response at the monitoring points of the high light pole structure under different windspeeds and different side plate height conditions are shown in Figure 25.

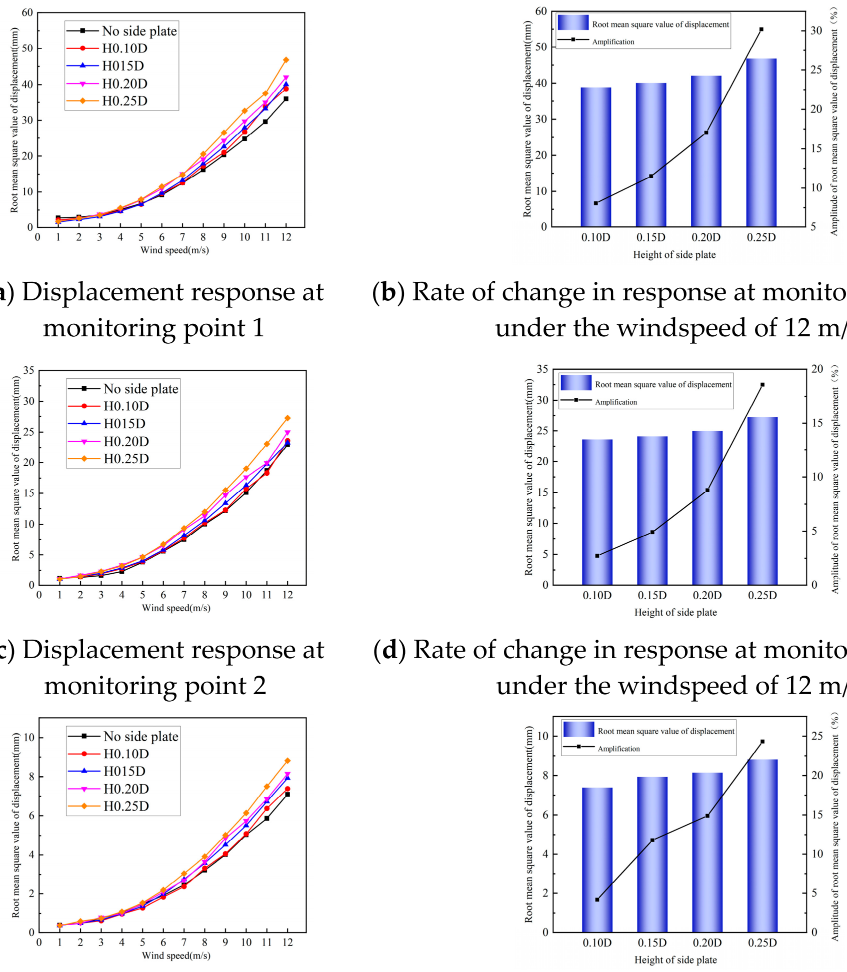


(**a**) Displacement response at monitoring point 1

(**b**) Rate of change in response at monitoring point 1 under the windspeed of 12 m/s

(**c**) Displacement response at monitoring point 2

(**d**) Rate of change in response at monitoring point 2 under the windspeed of 12 m/s

(**e**) Displacement response at monitoring point 3

(**f**) Rate of change in response at monitoring point 3 under the windspeed of 12 m/s

**Figure 25.** Root mean square value of the along-wind displacement response at the monitoring points of the high light pole structure under different side plate height conditions.

In Figure 25, we can clearly see that the along-wind root mean square displacement response of the light pole under different side plate height conditions expresses rather similar trends. In general, for the case in which the pitch is equal, the along-wind vibration responses of the structure continue to improve with increasing side plate height. When the incoming windspeed reaches 12 m/s, the root mean square value of the along-wind displacement of the pole without side plates reaches its maximum value. Similar to Figure 19, under the same windspeed of 12 m/s, the rate of change in responses at different monitoring points has varying degrees of increase.

### 4.5.2. Crosswind Response

Figure 26 represents the root mean square values of the crosswind displacement response at the monitoring points of the high light pole structure under different windspeeds and different side plate height conditions.

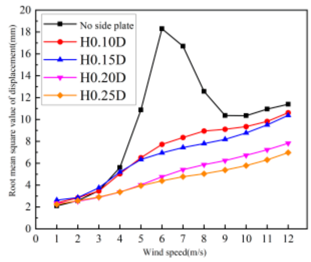


(**a**) Displacement response at monitoring point 1

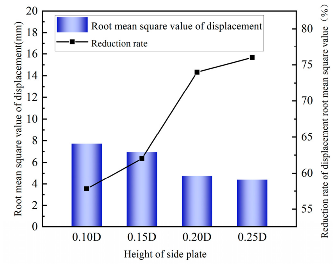


(**b**) Rate of change in response at monitoring point 1 under the windspeed of 6 m/s

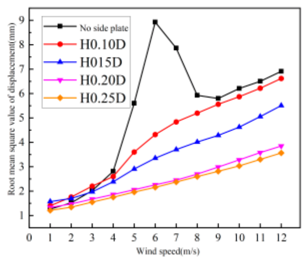


(**c**) Displacement response at monitoring point 2

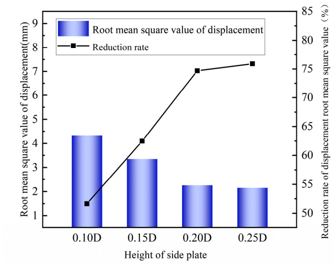


(**d**) Rate of change in response at monitoring point 2 under the windspeed of 6 m/s

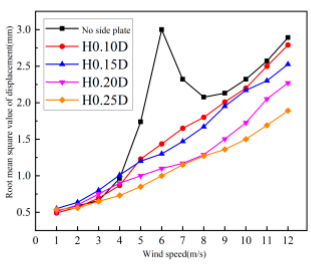


(**e**) Displacement response at monitoring point 3

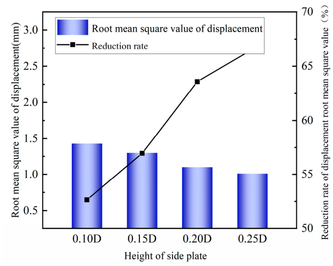


(**f**) Rate of change in response at monitoring point 3 under the windspeed of 6 m/s

**Figure 26.** Root mean square value of the crosswind displacement response at the monitoring points of the high light pole structure under different side plate height conditions.

Figure 26 shows that as the windspeed increases, the dynamic response of the light pole with spiral side plates increases regardless of the side plate height. A comparison of Figures 20 and 26 also indicates that no obvious vortex-induced vibration occurs, which proves once again that the spiral side plates have a good effect on suppressing crosswind vortex-induced vibration.

Similarly, when the windspeed is 12 m/s, the comparison of the amplification ratio of the along-wind displacement response of the light pole under different side plate height conditions is shown in Figure 27. For the crosswind displacement of the light pole, when the windspeed is 6 m/s, the comparison of the control ratio of the crosswind displacement response of the light pole under different side plate height conditions is demonstrated in Figure 28. The red line shown in Figures 27 and 28 has the same meaning as that shown in Figures 21 and 22, respectively.

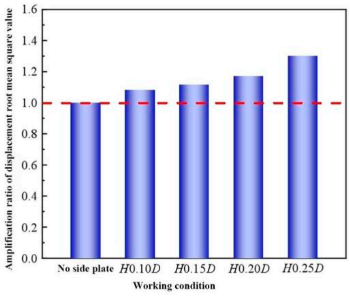


**Figure 27.** Along-wind displacement response at monitoring point 1 under a windspeed of 12 m/s and different side plate height conditions.

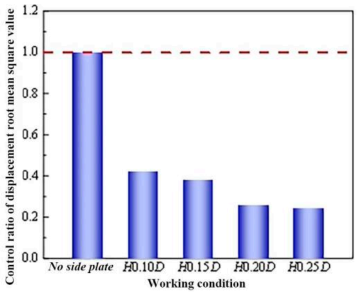


**Figure 28.** Crosswind displacement response at monitoring point 1 under a windspeed of 6 m/s and different side plate height conditions.

A comparison of Figures 27 and 28 shows that as the height of the side plate increases from 0.10 *D* to 0.25 *D*, the along-wind displacement response of the light pole gradually increases, whereas the crosswind displacement response of the light pole greatly decreases. Furthermore, as clearly demonstrated in Figures 27 and 28, the crosswind vibration attenuation effect of case P15D_H0.25D is slightly better than that of case P15D_H0.20D. However, the along-wind vibration amplification effect of case P15D_H0.25D is significantly larger than that of case P15D_H0.20D. Therefore, in practical engineering, the side plate height *H* = 0.20 *D* is a better choice for the design of vibration attenuation for similar high-mast light pole structures.

## 5. Conclusions

In this study, finite element models for high-mast light poles without and with spiral helical strakes are established. Based on a two-way fluid–structure interaction simulation method, the along-wind and crosswind dynamic responses of the high-mast light poles under different windspeeds are analyzed. The following are the main conclusions drawn from this study:

1. For high-mast light poles without spiral helical strakes, both the along-wind and crosswind vibration responses increase gradually with increasing windspeed in a wind environment. The along-wind acceleration response of the structure is dominated by the first-order vibration mode of the structure, whereas the crosswind acceleration response is mainly contributed by its high-order vibration mode. For the high-mast light poles presented in this paper, evident vortex-induced vibrations occur in the windspeed range of 5~8 m/s, especially when the incoming windspeed is 6 m/s;
2. For high-mast light poles with spiral helical strakes, as the pitch of the side plate decreases and the height of the side plate increases, the along-wind displacement response of the light pole gradually increases, whereas the crosswind displacement response greatly decreases;
3. In practical engineering, when spiral helical strakes are used for the design of high-mast light poles, the recommended values of the pitch *P* and the height of the side plate *H* are *P* = 7.5 *D* and *H* = 0.20 *D*, respectively.

**Author Contributions:** Conceptualization, M.Z. and G.Z.; methodology, M.Z., T.L. and Y.C.; software, M.Z. and G.Z.; validation, T.L., Y.W. and G.Z.; formal analysis, T.L., Y.W. and Y.C.; investigation, Y.W. and Y.C.; resources, M.Z. and G.Z.; data curation, T.L.; writing—original draft preparation, M.Z., T.L. and Y.C.; writing—review and editing, Y.W. and G.Z. All authors have read and agreed to the published version of the manuscript.

**Funding:** This research was funded by the National Natural Science Foundation of China (Grant no. 51578512) and the Cultivating Fund Project for Young Teachers of Zhengzhou University (Grant no. JC21539028).

**Institutional Review Board Statement:** Not applicable.

**Informed Consent Statement:** Not applicable.

**Data Availability Statement:** Data are contained within this article.

**Conflicts of Interest:** The authors declare no conflict of interest.

## References

1. Salahshoor, S.; Afzal, S. Subsurface technologies for hydrogen production from fossil fuel resources: A review and techno-economicanalysis. *Int. J. Hydrog. Energy* 2022, *in press*. [CrossRef]
2. Ahrens, J.; Geveci, B.; Law, C. Paraview: An end-user tool for large data visualization. *Vis. Handb.* **2005**, *717*, 50038-1.
3. Kasseh, Y.; Touzani, A.; El Majaty, S. What public lighting governance model should be deployed in Moroccan cities for sustainable and efficient energy management? *Mater. Today Proc.* **2022**, *72*, 3244–3252. [CrossRef]
4. Chao, G. Design and Experimental Research on Electromechanical System of BAGG01 High Pole Light. Master's Thesis, Southeast University, Nanjing, China, 2017.
5. Dexter, R.J.; Ricker, M.J. *NCHRP Report: Fatigue-Resistant Design of Cantilevered Signal, Sign, and Light Supports*; Transportation Research Board: Washington, DC, USA; National Research Council: Washington, DC, USA, 2002.
6. Sherman, R.J.; Hebdon, M.H.; Connor, R.J. Fatigue testing and retrofit details of high-mast lighting towers. *Eng. J.* **2016**, *53*, 61–72.
7. Chang, B.; Phares, B.; Sarkar, P.; Wipf, T. Development of a procedure for fatigue design of slender support structures subjected to wind-induced vibration. *Transp. Res. Rec. J. Transp. Res. Board* **2009**, *2131*, 23–33. [CrossRef]
8. Shen, S.; Yu, H.; Liu, J. Wind-induced vibration control of high pole lamp by rolling type modulation mass damping device. *J. Guangxi Univ.* **2018**, *43*, 1320–1328.
9. Caracoglia, L.; Jones, N.P. Numerical and experimental study of vibration mitigation for highway light poles. *Eng. Struct.* **2007**, *29*, 821–831. [CrossRef]
10. Bhoyar, D.C.; Vanalkar, A.V. Methodology for Design and Analysis of High Mast Solar Light Pole—A Review. *Int. J. Sci. Res. Dev.* **2015**, 27–29.
11. Zhuge, H.; Li, D. Study on the measurement of wind-induced vibration of 30 m high pole lamp. *Eng. Mech.* **1998**, *15*, 109–117.
12. Taplin, G.; Sanders, G.; Maklary, Z. Fatigue Failures of Light Poles. In Proceedings of the Austroads 6th Bridge Conference: Bridging the Gap, Perth, Australia, 12–15 September 2006.
13. Goode, J.S.; van de Lindt, J.W. Development of a semiprescriptive selection procedure for reliability-based fatigue design of high-mast lighting structural supports. *J. Perform. Constr. Facil.* **2007**, *21*, 193–206. [CrossRef]
14. Chien, C.W.; Jang, J.J. Case study of wind-resistant design and analysis of high mast structures based on different wind codes. *J. Mar. Sci. Technol.* **2008**, *16*, 6. [CrossRef]
15. Chang, B. Aerodynamic Parameters on a Multisided Cylinder for Fatigue Design. In *Wind Tunnels and Experimental Fluid Dynamics Research*; IntechOpen: Rijeka, Croatia, 2011.
16. Dawood, M.; Goyal, R.; Dhonde, H. Fatigue Life Assessment of Cracked High-Mast Illumination Poles. *J. Perform. Constr. Facil.* **2014**, *28*, 311–320. [CrossRef]
17. Peng, H.; Guo, J.; Chen, Z. Operation reliability analysis of high pole lamp under extreme weather conditions. *Sci. Technol. Econ. Guide* **2016**, *1*, 109–111.
18. Azzam, D.M. Fatigue Behavior of Highway Welded Aluminum Light Pole Support Structures. Ph.D. Thesis, University of Akron, Akron, OH, USA, 2006.
19. Sherman, R.J.; Connor, R.J. Development of a fatigue design load for high-mast lighting towers. *J. Struct. Eng.* **2018**, *145*, 04018228.1–04018228.8. [CrossRef]
20. Zhou, X.; Han, Y.; Yan, H. Research on vortex induced vibration and influencing factors of variable cross-section round lamp post based on wind tunnel test. *J. China Highw. Eng.* **2021**, *34*, 48–56.
21. Connor, R.J. *Fatigue Loading and Design Methodology for High-Mast Lighting Towers*; Transportation Research Board: Washington, DC, USA, 2012.
22. Thompson, R.W. Evaluation of High-Level Lighting Poles Subjected to Fatigue Loading. Master's Thesis, Lehigh University, Bethlehem, PA, USA, 2012.

23. Counsell, S.; Taplin, G.; Thomas, M. Fatigue Analysis and Repair of a High Mast Light Pole. In Proceedings of the Austroads 7th Bridge Conference, Auckland, New Zealand, 26–29 May 2009.
24. Zhou, G.; Ye, Z.; Li, C.; Yang, J.; Wang, D. Research on dynamic characteristics of floating wind turbines with spiral side plates. *J. Sol. Energy* **2017**, *38*, 2565–2573.
25. Zhang, N. Numerical study on forced oscillation of helical side plates with different cross section shapes. *Therm. Power Eng.* **2018**, *33*, 67–74.
26. Zhou, T.; Razali, S.; Hao, Z.; Cheng, L. On the study of vortex-induced vibration of a cylinder with helical strakes. *J. Fluids Struct.* **2011**, *27*, 903–917. [CrossRef]
27. Zhou, Y. Experimental study on two-way vortex-induced vibration of riser with spiral side plates. *Vib. Shock.* **2018**, *37*, 249–255.
28. Ranjith, E.R.; Sunil, A.S.; Pauly, L. Analysis of flow over a circular cylinder fitted with helical strakes. *Procedia Technol.* **2016**, *24*, 452–460. [CrossRef]
29. Quen, L.K.; Abu, A.; Kato, N.; Muhamad, P.; Abdullah, H. Investigation on the effectiveness of helical strakes in suppressing VIV of flexible riser. *Appl. Ocean. Res.* **2014**, *44*, 82–91. [CrossRef]
30. Chen, D.; Abbas, L.K.; Wang, G.P.; Rui, X.T.; Lu, W.J. Suppression of vortex-induced vibrations of a flexible riser by adding helical strakes. *J. Hydrodyn.* **2019**, *31*, 622–631. [CrossRef]
31. Aheran, E.B.; Puckett, J. *Reduction of Wind-Induced Vibrations in High-Mast Light Poles*; University of Wyoming: Laramie, WY, USA, 2010.
32. American Association of State Highway and Transportation Officials. *AASHTO Guide for Design of Pavement Structures*; The Association: Washington, DC, USA, 1993.
33. Braza, M.; Chassaing, P.; Minh, H.H. Numerical study and physical analysis of the pressure and velocity fields in the near wake of a circular cylinder. *J. Fluid Mech.* **1986**, *165*, 79–130. [CrossRef]
34. Kumar, R.A.; Sohn, C.H.; Gowda, B.H.L. Passive control of vortex-induced vibrations: An overview. *Recent Pat. Mech. Eng.* **2008**, *1*, 1–11. [CrossRef]